Journal of Thermal Biology 62 (2016) 201–209

Contents lists available at ScienceDirect

Journal of Thermal Biology

journal homepage: www.elsevier.com/locate/jtherbio

Thermoelastic modelling of the skin at finite deformations

A. McBride [a,d,*], S. Bargmann [b,c], D. Pond [d], G. Limbert [e,f]

[a] School of Engineering, University of Glasgow, United Kingdom
[b] Institute of Continuum Mechanics and Materials Mechanics, Hamburg University of Technology, Germany
[c] Institute of Materials Research, Helmholtz-Zentrum Geesthacht, Germany
[d] Centre for Research in Computational and Applied Mechanics, University of Cape Town, South Africa
[e] National Centre for Advanced Tribology at Southampton (nCATS)/ Bioengineering Science Research Group, Faculty of Engineering and the Environment, University of Southampton, United Kingdom
[f] Biomechanics and Mechanobiology Laboratory, Department of Human Biology, Faculty of Health Sciences, University of Cape Town, South Africa

ARTICLE INFO

Article history:
Received 27 November 2015
Accepted 28 June 2016
Available online 10 July 2016

ABSTRACT

The modelling and computation of the coupled thermal and mechanical response of human skin at finite deformations is considered. The model extends current thermal models to account for thermally- and mechanically-induced deformations. Details of the solution of the highly nonlinear system of governing equations using the finite element method are presented. A representative numerical example illustrates the importance of considering the coupled response for the problem of a rigid, hot indenter in contact with the skin.

1. Introduction

The skin is the largest organ in the human body. In addition to its multiple physiological functions (e.g. thermo-regulation, vitamin D synthesis, neurotransduction), the skin acts as a complex biophysical interface protecting the internal body structures from the external environment. The nature of these interfacial phenomena spans the mechanical, thermal, biological, chemical, radiological and electromagnetic domains (Burns et al., 2004; Limbert, 2014). The nonlinear interplay between these processes presents researchers with numerous challenges when attempting to develop a mechanistic understanding of skin physiology in health, disease and trauma.

As depicted in Fig. 1, the skin can be divided roughly into four main layers: the stratum corneum, viable epidermis, dermis and hypodermis. Each of these layers has a complex micro-architecture and distinct material properties. The skin thickness varies according to body location from approximately 0.5–4 mm.

The need to develop robust and predictive thermomechanical models of human skin is largely motivated by recent applications in medical therapies. These include temperature-based disease diagnostics, cryotherapy, cryosurgery, infra-red light therapy, heat plasters, cancer hyperthermia, and laser surgery, among others (see (Xu et al., 2008; Xu and Lu, 2011) for extensive reviews of skin biothermomechanics). These models need to account for the complex anatomical structure of skin, blood perfusion and the nonlinear coupled thermal and mechanical response of the system. Further areas where thermomechanical models of the skin have potential application are briefly described in the subsequent paragraphs.

The skin is constantly subjected to a wide range of thermo-mechanical interactions with the environment over the duration of a human life. The coupling between thermal effects and mechanical loadsand, ultimately, biochemical processes of particular relevance to the formation of pressure ulcers and skin blisters (Knapik et al., 1995; Sulzberger et al., 1966). For such applications an understanding of skin microclimate is key (Gefen, 2011). It is therefore essential to gain a mechanistic understanding of how thermal exchanges in combination with relative humidity and mechanical stress can accelerate the occurrence of skin breakdown. Over the last few decades there has been a tremendous surge in the practice of tattooing as a cosmetic, decorative and social body art form (Khunger et al., 2015). As a corollary of this surge, the number of people seeking to have tattoos removed has grown significantly (Kuperman-Beade et al., 2001). Currently, the most efficient removal techniques rely on the use of Q-switched lasers which work on the principle of selective photothermolysis (Choudhary et al., 2010; Kuperman-Beade et al., 2001). The tattoo pigments are destroyed by targeting their absorption wave length with a laser pulse duration shorter that the thermal relaxation time (i.e. the time required for a structure to cool down to half of its heating temperature). Despite these technical precautions, the

* Corresponding author at: School of Engineering, University of Glasgow, United Kingdom
E-mail addresses: andrew.mcbride@glasgow.ac.uk (A. McBride), swantje.bargmann@tu-harburg.de (S. Bargmann), damien.pond@uct.ac.za (D. Pond), g.limbert@soton.ac.uk (G. Limbert).

http://dx.doi.org/10.1016/j.jtherbio.2016.06.017

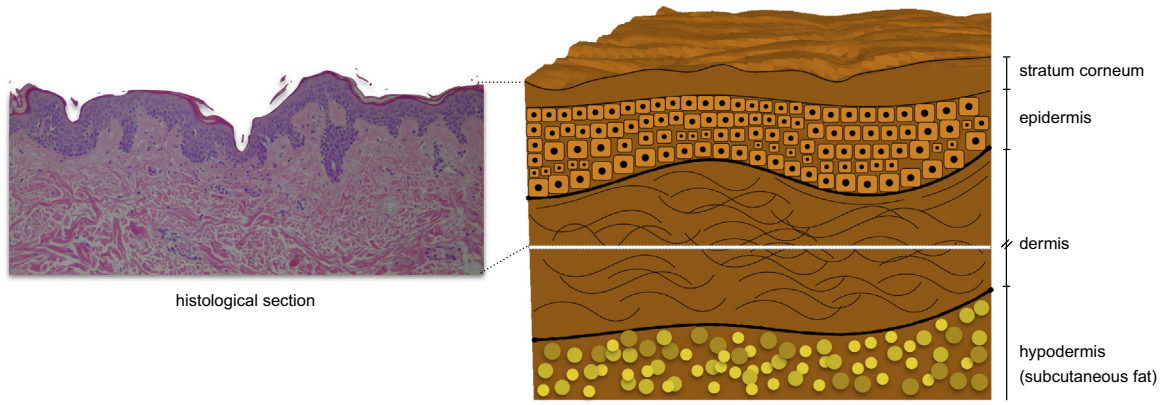

Fig. 1. A schematic of the various layers that comprise the skin and a histological section (section courtesy of Maria Fabiola Leyva-Mendivil, University of Southampton).

thermal and subsequent photochemical effects of laser exposure on the epidermis and dermis are not without side effect (e.g. dyspigmentation and textural changes due to melanin which has absorption wave lengths overlapping those of the targeted tattoo pigments, rupture of blood vessels and aerosolization of tissue, potential carcinogenicity). A better understanding of how heat phenomena operate within the highly-deformable multiphasic and multiscale structure of the skin is thus required. Other side effects of tattoos include skin burns during MRI acquisition procedures (Kreidstein et al., 1997; Ross and Matava, 2011). These burns result from an electromagnetic reaction to the ferromagnetic metallic compounds found in tattoo pigments. This effectively induces an electric current that heats skin tissue.

It is clear that developing a mechanistic understanding of the physiology of heat generation and heat transfer across the skin is of considerable interest. Predictive computational models are likely to play an increasing role in the future by allowing hypothesis-driven, physics-based research. Sound and thermodynamically-consistent theoretical and associated numerical models of thermomechanical phenomena in skin are therefore urgently needed. They should also account for the complex anatomical structure of skin, blood perfusion and the nonlinear coupled thermal and mechanical response of the system.

Mechanical models of human skin at various length scales are well developed (see (Querleux, 2014) for an extensive overview). For a review on constitutive models for skin biomechanics, see Limbert (2014). At the macroscopic scale (the scale at which one approximates the skin as a continuum) sophisticated constitutive relations that capture the near-incompressible nature of tissue and the directional properties of the collagen fibres for finite deformations in three dimensions are well established (see e.g. (Bischoff et al., 2000, 2002; Limbert, 2011; Tepole et al., 2012) and the references therein). These models are highly nonlinear and require numerical methods to obtain approximate solutions.

Thermal models for heat transfer accounting for biological heat sources in the skin are also relatively well developed. In particular, Pennes (1948) model of heat conduction is widely used to describe biological heat transfer in human tissue (see e.g. (Lang et al., 1999; Shen et al., 2005; Ratovoson et al., 2011)) with applications in therapeutic hyperthermia and burn damage, among others (see (Xu and Lu, 2011) for an extensive review). The Pennes (1948) model in its original form has the structure of the linear heat equation with physiologically motivated heat supply terms accounting for perfusion (the physiological process of blood delivery to biological tissue), metabolism and external heat sources. Various nonlinear extensions of Pennes model have been proposed to account for the temperature dependence of the perfusion rate (see e.g. (Lakhssassi et al., 2010; Lang et al., 1999)). Hassanpour and Saboonchi (2014) presented a comparison of Pennes model with more recent proposals in the literature.

Coupled thermomechanical models of human skin, where the coupled mechanical and thermal response is considered, are by comparison relatively basic. In such models the skin is generally assumed to be a rigid conductor and the stress due to thermal loading obtained in a post-processing step. The assumption of a linear elastic response is normally made to compute the stress from the thermally induced strains. These models are generally restricted to one or two space dimensions. The numerical solution of such models has been achieved using a variety of different techniques. Ghazanfarian et al. (2015) solved the nonlinear one-dimensional Pennes nmodel using a meshless particle method. Meshless methods present no obvious advantage over more established, mesh-based methods for such applications however. Bedin and Bazán (2014) constructed a series solution for the two-dimensional problem with convective boundary conditions. The spectral element method was used by Dehghan and Sabouri (2012) to determine the heat distribution in two dimensions for healthy tissue and tissue containing a tumour. Zhao et al. (2005) used a two level finite difference scheme for the one-dimensional Pennes model. Shen et al. (2005) coupled the Pennes model to linear elasticity via a thermal stress contribution. The influence of the deformation on temperature evolution was ignored. Lang et al. (1999) used an adaptive three-dimensional finite element model to approximate a nonlinear extension of Pennes model (temperature-dependent blood perfusion) to develop an optimisation treatment for regional hyperthermia of deep-seated tumours. In addition to performing an impressive experimental investigation of heat transfer in the skin, Ratovoson et al. (2011) developed a finite element model to examine the response in the vicinity of a vein where the outer surface of the skin is exposed to a heat source. The blood flow in the artery was approximated using the Navier–Stokes equations and the Pennes model applied to the surrounding tissue. Xu et al. (2008) investigated thermal damage due to surface heating and microwave radiation for a two-dimensional, three-layer model of human skin incorporating the Pennes model. While a range of methods have been used to solve the problem of heat conduction in skin, the finite element method would appear to be the natural choice as it is well developed and can handle arbitrary geometries and nonlinearities.

The focus of the current presentation is on developing a robust predictive numerical model for the coupled thermomechanical response of the skin at finite deformations. That is, a model that accounts for geometric and material nonlinearities associated with the assumption of finite deformations and nonlinear constitutive laws (both mechanical and thermal). The numerical model also extends Pennes (1948) model to the finite deformation regime. The need to account for finite deformations is provided by the relatively significant deformations that the skin can undergo due

the application of a thermal treatment device or due to tumour growth, for example. Furthermore, much of the loading that skin experiences is not in the infinitesimal regime.

The highly nonlinear system of governing equations are solved using the finite element method in conjunction with an iterative Newton–Raphson scheme. Automatic differentiation tools (Korelc, 2002) are employed to facilitate the computations of the tangent matrices required in the Newton scheme. These tools have great potential for developing robust numerical models in biomechanics as they largely remove sources of error that arise when linearising complex nonlinear systems.

The structure of the presentation is as follows. The notation and basic relations are first introduced. The kinematic descriptors of the deformation are briefly summarised in Section 2. This is followed by the statement of the governing system of geometrically nonlinear equations. The constitutive relations are summarised in Section 4. The extension of the Pennes (1948) model to the finite deformation regime is given. The weak form of the governing relations and details of the finite element strategy used to solve them are then presented. A numerical example is presented in Section 6 to elucidate aspects of the formulation.

Notation and basic relations

Direct notation is adopted throughout. Occasional use is made of index notation, the summation convention for repeated indices being implied. The scalar product of two vectors $\boldsymbol{a}$ and $\boldsymbol{b}$ is denoted $\boldsymbol{a}\cdot\boldsymbol{b} = [\boldsymbol{a}]_i[\boldsymbol{b}]_i$. The scalar product of two second-order tensors $\boldsymbol{A}$ and $\boldsymbol{B}$ is denoted $\boldsymbol{A}\colon\boldsymbol{B} = [\boldsymbol{A}]_{ij}[\boldsymbol{B}]_{ij}$. The composition of two second-order tensors $\boldsymbol{A}$ and $\boldsymbol{B}$, denoted $\boldsymbol{AB}$, is a second-order tensor with components $[\boldsymbol{AB}]_{ij} = [\boldsymbol{A}]_{im}[\boldsymbol{B}]_{mj}$. The tensor product of two vectors $\boldsymbol{a}$ and $\boldsymbol{b}$ is a second-order tensor $\boldsymbol{D} = \boldsymbol{a}\otimes\boldsymbol{b}$ with $[\boldsymbol{D}]_{ij} = [\boldsymbol{a}]_i[\boldsymbol{b}]_j$. The action of a second-order tensor $\boldsymbol{A}$ on a vector $\boldsymbol{b}$ is a vector with components $[\boldsymbol{a}]_i = [\boldsymbol{A}]_{im}[\boldsymbol{b}]_m$.

2. Kinematics

The fundamental kinematic measures used to quantify the motion and deformation of the skin as a continuum body are now presented. For additional information the reader is referred to the reference works by Gurtin (2003); Holzapfel (2000), among others.

Consider a continuum body taken to represent the skin whose placement in the reference configuration is denoted $\mathcal{V}_0$ at time $t=0$, as shown in Fig. 2. The boundary of the domain in the reference configuration is denoted by $\partial\mathcal{V}_0$, with outward unit normal $\boldsymbol{N}$. A typical material point within the reference configuration is identified by the position vector $\boldsymbol{X}$. The observed configuration of the body at a later time t is denoted $\mathcal{V}$ with a typical material point identified by the position vector $\boldsymbol{x}$. The absolute temperature is defined by $\vartheta = \tilde{\vartheta}(\boldsymbol{X}, t)$ and the initial temperature at time $t=0$ is denoted by ϑ_0. The motion $\boldsymbol{\varphi}$ relates the observed and reference configurations as $\boldsymbol{x} = \boldsymbol{\varphi}(\boldsymbol{X}, t)$. The deformation gradient is defined as the derivative of the motion $\boldsymbol{\varphi}$ with respect to the reference configuration; that is,

$$\boldsymbol{F}(\boldsymbol{X}, t) := \mathrm{Grad}\boldsymbol{\varphi}(\boldsymbol{X}, t),$$

where $\mathrm{Grad}(\bullet) := \partial(\bullet)/\partial\boldsymbol{X}$. The Jacobian determinant of the deformation gradient is denoted by $J := \det\boldsymbol{F} > 0$. The right Cauchy–Green stretch tensor is defined by $\boldsymbol{C} := \boldsymbol{F}^{\mathrm{T}}\boldsymbol{F}$.

3. Governing relations

The balance of various fundamental measures is employed to determine the governing relations used to approximate the response of the skin to applied loading. For an excellent overview of the derivation of these fundamental relations, the reader is referred to Beradi et al. (1996).

The balance of linear momentum in the absence of inertial forces (i.e. the equilibrium equation) and the Neumann boundary condition for the first Piola–Kirchhoff traction vector $\boldsymbol{T}$ are given by

$$\mathrm{Div}\boldsymbol{P} + \boldsymbol{b}_0 = \boldsymbol{0} \quad \text{in } \mathcal{V}_0, \tag{1}$$

$$\boldsymbol{T} \equiv \boldsymbol{T}^{\mathrm{p}} = \boldsymbol{PN} \quad \text{on } \partial\mathcal{V}^{\boldsymbol{\varphi}}_{0,\mathrm{N}}, \tag{2}$$

where $\boldsymbol{P}$ is the first Piola–Kirchhoff stress tensor, $\boldsymbol{b}_0$ is the reference body force, and $\boldsymbol{T}^{\mathrm{p}}$ is the prescribed first Piola–Kirchhoff traction vector acting on the Neumann part of the boundary $\partial\mathcal{V}^{\boldsymbol{\varphi}}_{0,\mathrm{N}} \subset \partial\mathcal{V}_0$. Dirichlet boundary conditions on the motion $\boldsymbol{\varphi}$ are prescribed on $\partial\mathcal{V}^{\boldsymbol{\varphi}}_{0,\mathrm{D}}$, where $\partial\mathcal{V}_0 = \partial\mathcal{V}^{\boldsymbol{\varphi}}_{0,\mathrm{N}} \cup \partial\mathcal{V}^{\boldsymbol{\varphi}}_{0,\mathrm{D}}$ and $\partial\mathcal{V}^{\boldsymbol{\varphi}}_{0,\mathrm{N}} \cap \partial\mathcal{V}^{\boldsymbol{\varphi}}_{0,\mathrm{D}} = \varnothing$.

The temperature evolution equation arising from the first law of thermodynamics and the Neumann boundary condition are given by

$$c_{\boldsymbol{F}}\dot{\vartheta} = -\,\mathrm{Div}\boldsymbol{Q} + Q - H_e \quad \text{in } \mathcal{V}_0, \tag{3}$$

$$Q^{\mathrm{p}} = \boldsymbol{Q}\cdot\boldsymbol{N} = h\Big[\boldsymbol{N}\cdot\boldsymbol{C}^{-1}\boldsymbol{N}\Big]^{1/2}\big[\vartheta - \vartheta_\infty\big] \quad \text{on } \partial\mathcal{V}^{\vartheta}_{0,\mathrm{N}}, \tag{4}$$

where

$$H_e := -\,\vartheta\frac{\partial\boldsymbol{P}}{\partial\vartheta}\colon\dot{\boldsymbol{F}} \tag{5}$$

accounts for thermoelastic coupling effects, and $c_{\boldsymbol{F}}$ is the specific heat capacity at constant deformation. The first Piola–Kirchhoff heat flux vector is denoted by $\boldsymbol{Q}$, and Q denotes the rate of heat

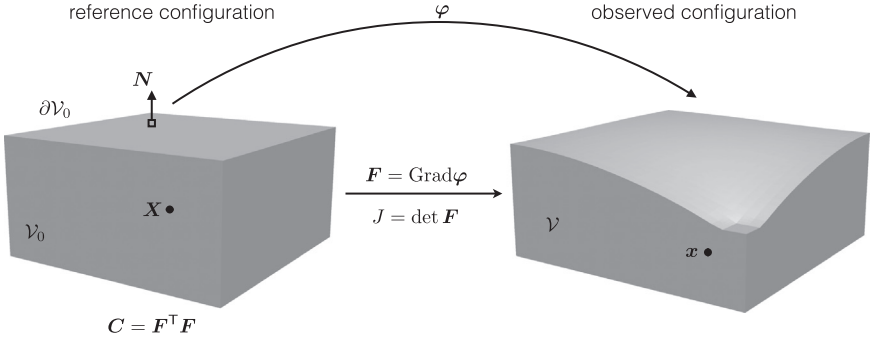

Fig. 2. The motion of the continuum body and the various kinematic descriptors used to describe the deformation.

source per unit reference volume. The final term in the Neumann boundary condition (4) accounts for Newton cooling with the external environment. The spatial heat transition coefficient is denoted by h. The area ratio $[\boldsymbol{N}\cdot\boldsymbol{C}^{-1}\boldsymbol{N}]^{1/2}$ accounts for the change in area from the observed to the reference configuration, and ϑ_∞ is the external temperature. The presence of the area ratio in the Neumann boundary condition arises from the assumption of finite deformations.

4. Constitutive relations

The structure of the constitutive relations are derived from, or suggested by, the second law of thermodynamics. We choose to omit their derivations for the sake of brevity.

4.1. Structure of the free energy and the stress

As is clear from Fig. 1, the skin has multiple layers and a complex microstructure. Microstructurally-motivated, hyper-elastic, worm-like chain models for the collagen fibres in the dermis and a near-incompressible isotropic model for the ground substance (see e.g. (Bischoff et al., 2002; Garikipati et al., 2004; Tepole et al., 2012)) are widely used to approximate the mechanical response. An extension of these models to account for thermal effects appears lacking and warrants further investigation. Given this, the constitutive response of the skin to loading will be approximated using a macroscopic hyper-thermoelastic model.

The free energy density $\Psi = \hat{\Psi}\big(\boldsymbol{F}, \vartheta\big)$ serves as a potential for the stress $\boldsymbol{P} = \tilde{\boldsymbol{P}}\big(\boldsymbol{F}, \vartheta\big)$ and the entropy $\eta = \tilde{\eta}(\boldsymbol{F}, \vartheta)$, which are given by the thermal equations of state as follows

$$\boldsymbol{P} = \frac{\partial \Psi}{\partial \boldsymbol{F}} \quad \text{and} \quad \eta = -\frac{\partial \Psi}{\partial \vartheta}. \tag{6}$$

The neoHookean type free energy employed here is given by

$$\Psi(\boldsymbol{F}, \vartheta) = \frac{1}{2}\lambda \ln^2 J + \frac{1}{2}\mu\big[\boldsymbol{F}\colon\boldsymbol{F} - 3 - 2\ln J\big] - 3\alpha\kappa\big[\vartheta - \vartheta_0\big]\frac{\ln J}{J} + c_{\boldsymbol{F}}\left[\vartheta - \vartheta_0 - \vartheta \ln\left(\frac{\vartheta}{\vartheta_0}\right)\right] - \Xi_0\big[\vartheta - \vartheta_0\big], \tag{7}$$

where λ and μ are the Lamé parameters, α is the thermal expansion coefficient, $\kappa := \lambda + (2/3)\mu$ is the bulk modulus, and Ξ_0 is the material specific absolute entropy. Hence, from Eq. 6, $\boldsymbol{P}$ is given by

$$\boldsymbol{P} = \big[\lambda \ln J - \mu\big]\boldsymbol{F}^{-\mathrm{T}} + \mu\boldsymbol{F} - 3\alpha\kappa\frac{1}{J}\big[\vartheta - \vartheta_0\big]\big[1 - \ln J\big]\boldsymbol{F}^{-\mathrm{T}}. \tag{8}$$

4.2. Duhamel's law of heat conduction

The structure of the first Piola–Kirchhoff heat flux vector $\boldsymbol{Q}$ follows from satisfying the heat conduction inequality via Duhamel's law of heat conduction and, assuming isotropic conductivity, takes the form

$$\boldsymbol{Q} = -k_0\boldsymbol{C}^{-1}\mathrm{Grad}\vartheta, \tag{9}$$

where k_0 is the material thermal conductivity and is related to the spatial thermal conductivity k as $k_0 = Jk$.

4.3. Heat supply according to Pennes model

The macroscopic biological heat conduction model of Pennes accounts for physiological factors such as metabolism and perfusion through heat supply (source) terms. The heat supply per unit current volume is denoted by q and is related to its material counterpart Q as $Q = Jq$. The heat supply q is assumed to take the form:

$$q := q_{\mathrm{per}} + q_{\mathrm{met}} + q_{\mathrm{ext}},$$

where q_{per}, q_{met} and q_{ext} are the contributions to heat supply from perfusion, metabolism and external sources, respectively.

Pennes (1948) argued that blood enters the tissue at arterial temperature ϑ_{art} and reaches tissue temperature ϑ before leaving the arterial system. Contributions to heating due to perfusion q_{per} are thus assumed to be given by

$$q_{\mathrm{per}} = w^{\mathrm{b}}c_{\mathrm{b}}[\vartheta_{\mathrm{art}} - \vartheta],$$

where w^{b} is the constant blood perfusion flow rate (i.e. the mass flow rate of blood per unit volume of tissue), c_b is the specific heat of blood. Pennes model of perfusion has been extended by various authors (see e.g. (Lang et al., 1999)) but the original form is adopted here.

The heat generated from metabolic processes in the tissue q_{met} has either been ignored (Lang et al., 1999), assumed constant (Shen et al., 2005), or a functional form suggested (Ratovoson et al., 2011).

External sources of heat supply q_{ext} can include electromagnetic radiation (see e.g. (Lang et al., 1999)), but are ignored here.

5. Weak form of governing equations and numerical implementation

The weak form of the governing Eqs. (1) and (3) and their respective boundary conditions (2) and (4) forms the basis for their approximate solution using the finite element method. The weak form of the equilibrium equation is obtained by contracting (1) with an arbitrary admissible motion $\delta\boldsymbol{\varphi}$, integrating the result over the reference configuration $\mathcal{V}_0$ and applying an integration by parts, which yields

$$R_{\boldsymbol{\varphi}} := \int_{\mathcal{V}_0} \mathrm{Grad}\delta\boldsymbol{\varphi}\colon\boldsymbol{P}\mathrm{d}V - \int_{\mathcal{V}_0}\delta\boldsymbol{\varphi}.\,\boldsymbol{b}_0\mathrm{d}V - \int_{\partial\mathcal{V}^{\boldsymbol{\varphi}}_{0,\mathrm{N}}}\delta\boldsymbol{\varphi}\cdot\boldsymbol{T}^{\mathrm{p}}\mathrm{d}A = 0, \tag{10}$$

where $R_{\boldsymbol{\varphi}}$ is the residual for the equilibrium equation. Following a near identical procedure, the weak form of the heat Eq. (3) yields the residual equation as

$$R_{\vartheta} := \int_{\mathcal{V}_0}\delta\vartheta c_{\boldsymbol{F}}\dot{\vartheta}\mathrm{d}V - \int_{\mathcal{V}_0}\mathrm{Grad}\delta\vartheta\cdot\boldsymbol{Q}\mathrm{d}V - \int_{\mathcal{V}_0}\delta\vartheta Q\mathrm{d}V + \int_{\mathcal{V}_0}\delta\vartheta H\mathrm{d}V + \int_{\partial\mathcal{V}^{\vartheta}_{0,\mathrm{N}}}\delta\vartheta Q^{\mathrm{p}}\mathrm{d}A = 0, \tag{11}$$

where $\delta\vartheta$ is an arbitrary admissible temperature variation.

The highly nonlinear coupled system of Eqs. (10)–(11) governing the response of the skin are solved approximately using the finite element method in space in conjunction with a global Newton–Raphson procedure. The finite element method naturally accommodates complex geometries and spatially varying constitutive parameters. The finite element library AceGen (Korelc, 2002) is used to implement the solution scheme. Automatic differentiation is used to compute the system of residual equations (the weak form of the governing relations) and the corresponding tangent (required for the Newton–Raphson scheme). A time-step duration control procedure is used to optimise the time-step size and to ensure quadratic convergence of the Newton–Raphson scheme. The domain is discretized using Lagrangian $Q1$ elements. A fully-implicit backward-Euler scheme is used to approximate the

time derivative present in Eq. 3.

The use of automatic differentiation for applications in solid biomechanics is extremely attractive as the complexity of the problem generally lies in the highly-nonlinear nature of the constitutive relations. Automatic differentiation removes many possible sources of error during the implementation of the tangents required for the Newton–Raphson procedure.

6. Numerical example

The theory developed in the preceding sections is elucidated using a three-dimensional numerical example. Consider the four-layer skin model illustrated in Fig. 3. The model is an approximation of the geometry depicted in Fig. 1. We have assumed here, for the sake of simplicity, that the surface of the skin is flat and that the interfaces between the various layers are flat and distinct. Such assumptions are made to focus attention on the thermo-mechanical response and are not restrictions of the method. The material properties, taken from Xu and Lu (2011), are given in Table 1. A two-dimensional rigid variant of the problem was examined by Xu and Lu (2011).

Various features of the theory developed in the preceding sections are now investigated by considering restrictions to what is termed here *the full model*. In the full model, a $24 \times 24 \times 6$ mm^3 sample of skin is compressed by a 2×2 mm^2 flat, rigid indenter. The temperature of the skin is initially prescribed to be the same as the core temperature $\vartheta_{\text{core}} = 37$ °C, while the initial temperature of the indenter is 90°. Contact is modelled by prescribing the vertical displacement of the nodes on the upper surface of the finite element mesh below the contact area. The contact is assumed frictionless. The indenter compresses the surface of the skin specimen a distance of 3 mm in the negative $\boldsymbol{e}_3$ (vertical) direction. The indentation is applied uniformly over a period of 25 s (termed stage I). The indenter is then retracted to its original location over a period of 25 s (termed stage II). The temperature of the indenter during the indentation process is fixed at 90 °. The temperature of the indenter is instantaneously reduced to ϑ_{core} at the onset of the retraction of the indenter (after 25 s).

Due to the geometric symmetry, only a quarter of the problem is modelled. The lateral boundaries of the domain are free to move in the vertical direction but are otherwise mechanically constrained. A homogeneous Neumann flux, i.e. $Q^{\text{p}} \equiv 0$, is assumed on the lateral boundaries. The part of the upper surface that is not in contact with the indenter undergoes (Newton) cooling with the external surroundings, with the external temperature set at $\vartheta_{\text{ext}} = 25$ °C. Note that, for the sake of ease of implementation, we have not considered the geometric nonlinearity in the Neumann boundary condition (4).

The domain is discretised into $24 \times 24 \times 36$ elements. The upper surface of the stratum corneum is further refined into 72×72 elements. The maximum permissible time-step size is 0.5 s. The time-step size is automatically decreased should the Newton scheme experience convergence problems.

6.1. Thermally- and mechanically-driven problem (the full model)

The variation in the temperature, the norm of the Cauchy stress tensor $\boldsymbol{\sigma} := J^{-1}\boldsymbol{P}\boldsymbol{F}^{\text{T}}$ and the norm of the Green–Lagrange strain tensor $\boldsymbol{E} := [1/2][\boldsymbol{C} - \boldsymbol{I}]$ at the end of stage I are shown in Fig. 4 (a)–(c). The variation in the temperature difference $\vartheta - \vartheta_{\text{core}}$ (that is, the difference between the current and initial temperature) at the centre of the various layers of the skin along the vertical line A–B (see Fig. 3) is shown in Fig. 4 (d).

Changes in temperature are fairly localised to the region in the vicinity of the indenter as is clear from Fig. 4 (a). The norm of the Cauchy stress is orders of magnitude higher in the stratum corneum compared to the rest of the specimen. This is due to the considerable variation in the Youngs modulus between the layers (see Table 1). As shown in Fig. 4 (c), the subcutaneous fat layer undergoes considerable strain due to the relatively low value of the Youngs modulus. The stratum corneum is acting as a relatively-rigid membrane placed over a highly-deformable domain primarily composed of the dermis and the subcutaneous fat.

As shown in Fig. 4 (d), the temperature in the stratum corneum is nearly instantaneously identical to that of the indenter. This is due to the very small thickness of the layer. All layers experience heating during stage I of loading. The delay in the heating response of the layers is due to the varying thickness of the layers and competition with the prescribed boundary condition at the lower boundary of the subcutaneous fat layer. The temperature at the centre of stratum corneum and the epidermis have reached an equilibrium state by the end of load stage I. The temperature at the centre of the dermis is still increasing at the end of stage I but the rate of increase is decreasing.

Relative cooling occurs during stage II of the loading. The temperature at the centre of the stratum corneum and the epidermal layers rapidly approaches the indenter temperature of ϑ_{core}. The temperature in the dermal layer decreases immediately at the beginning of stage II. This is not the case for the subcutaneous fat layer which continues increasing in temperature for a couple of seconds.

The overall thermomechanical response of the skin is further complicated due to the presence of Newton cooling with the

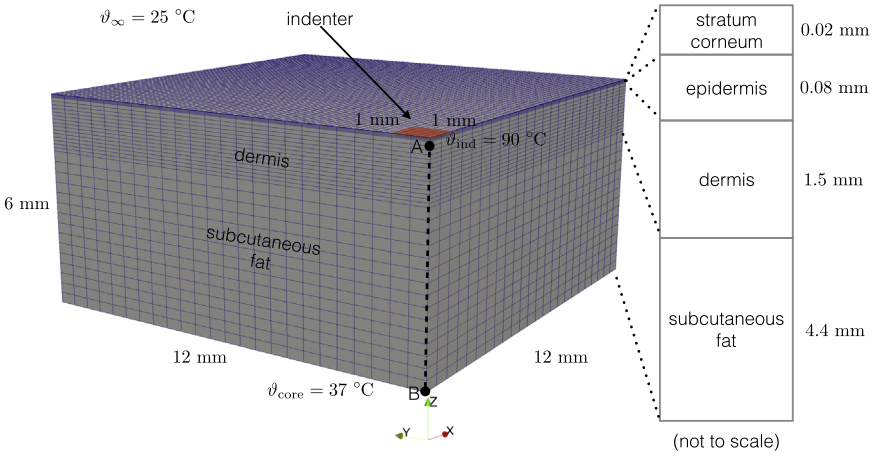

Fig. 3. A quarter of the domain showing the four layers that comprise the skin model. The thickness of the layers is also indicated.

Table 1
Constitutive parameters used for the numerical examples unless stated otherwise. The Young's modulus and the Poisson's ratio can be expressed in terms of the Lamé parameters as $\lambda = E\nu/(1+\nu)(1-2\nu)$ and $\mu = E/2(1+\nu)$. The specific heat capacity c_F is related to the heat capacity c by $c_F = \rho c$. The interface conductivity is given by $h = 0.008$ [N/mm s K].

Skin:						
			Stratum corneum	Epidermis	Dermis	Subcutaneous fat
Young's modulus	E	[N/mm^2]	1998	102	10.2	0.0102
Poisson's ratio	ν	[–]	0.48	0.48	0.48	0.48
Density	ρ	[kg/mm^3]	1500×10^{-9}	1190×10^{-9}	1116×10^{-9}	971×10^{-9}
Conductivity	k_0	[N/sK]	0.235	0.235	0.445	0.185
Heat capacity	c	[Nmm/kgK]	3600×10^3	3600×10^3	3300×10^3	2700×10^3
Blood perfusion	w^b	[kg/sm^3]	0	0	0.00125	0.00125
Metabolic supply	q_{met}	[N/mm^{2}s]	368.1×10^{-6}	368.1×10^{-6}	368.1×10^{-6}	368.1×10^{-6}

Blood:			
Density	ρ	[kg/mm^3]	1060×10^{-9}
Heat capacity	c	[Nmm/KgK]	3770×10^3

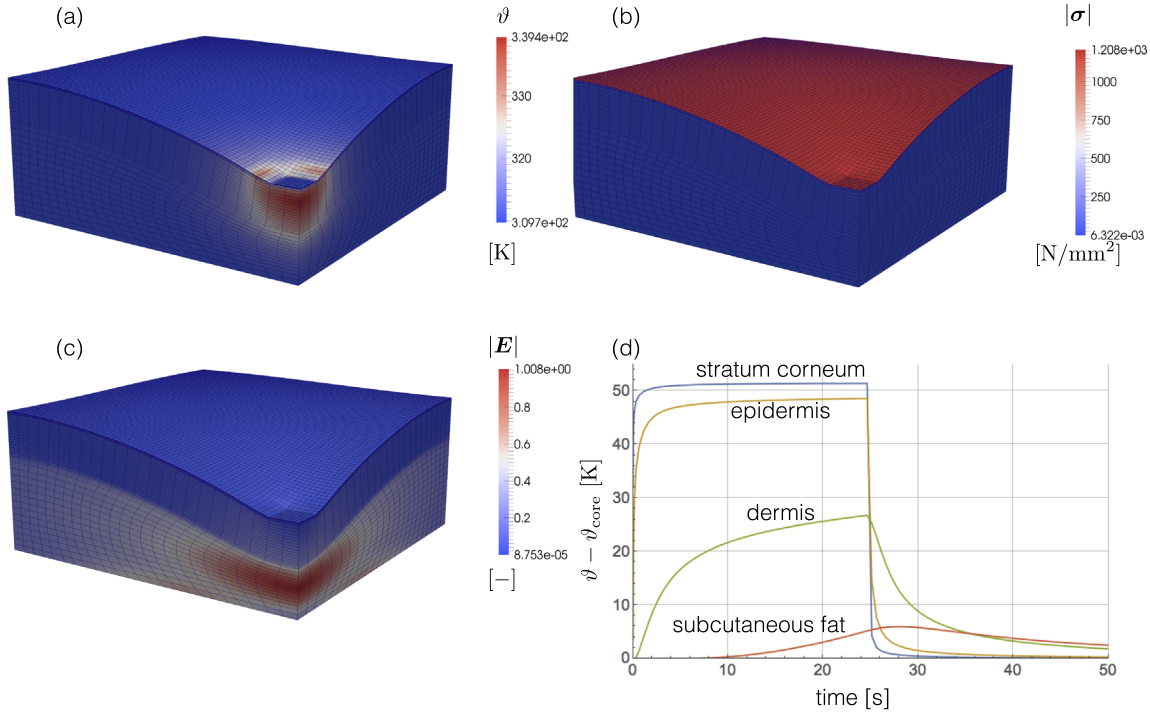

Fig. 4. The variation in the temperature ϑ, the norm of the Cauchy stress tensor $\boldsymbol{\sigma}$ and the norm of the Green–Lagrange strain tensor $\boldsymbol{E}$ at the end of loading stage I are shown in (a)-(c) for the full problem. The variation in the temperature difference $\vartheta - \vartheta_{core}$ at the centre of the various layers of the skin along the vertical line A–B is shown in (d).

environment on the upper surface and metabolic heat generation in the dermis and subcutaneous fat layers.

It is clear from the numerical results that the stratum corneum can play a significant role in the mechanical response of the skin model and should not be omitted.

6.2. Thermally-driven problem

The objective of the thermally-driven example is to examine the role that the imposed thermal loading has on the overall response by removing the mechanical loading from the problem. The indenter is therefore prevented from displacing during the simulation. The applied thermal loading remains the same.

The variation in the temperature, the norm of the Cauchy stress tensor and the norm of the Green–Lagrange strain tensor are once again shown in Fig. 5 (a)–(c). The variation in the temperature difference $\vartheta - \vartheta_{core}$ at the centre of the various layers of the skin along the vertical line A–B is shown in Fig. 5 (d).

The temperature variation in the domain during the heating phase (stage I) is generally similar to that of the full problem, thereby suggesting that the heating due to thermomechanical coupling is small. That this should be the case is not surprising given the very low value of the thermomechanical expansion coefficient α (see Eq. (7)) and the low applied loading rates. The temperature variation in the subcutaneous fat layer however differ significantly from that of the full problem. This is due to the influence of the mechanical deformation on the conduction (see Eq. (9)). Thus while it appears reasonable to exclude the thermomechanical coupling term H_e in the balance of energy (3), the mechanical contribution to the effective thermal conductivity (via

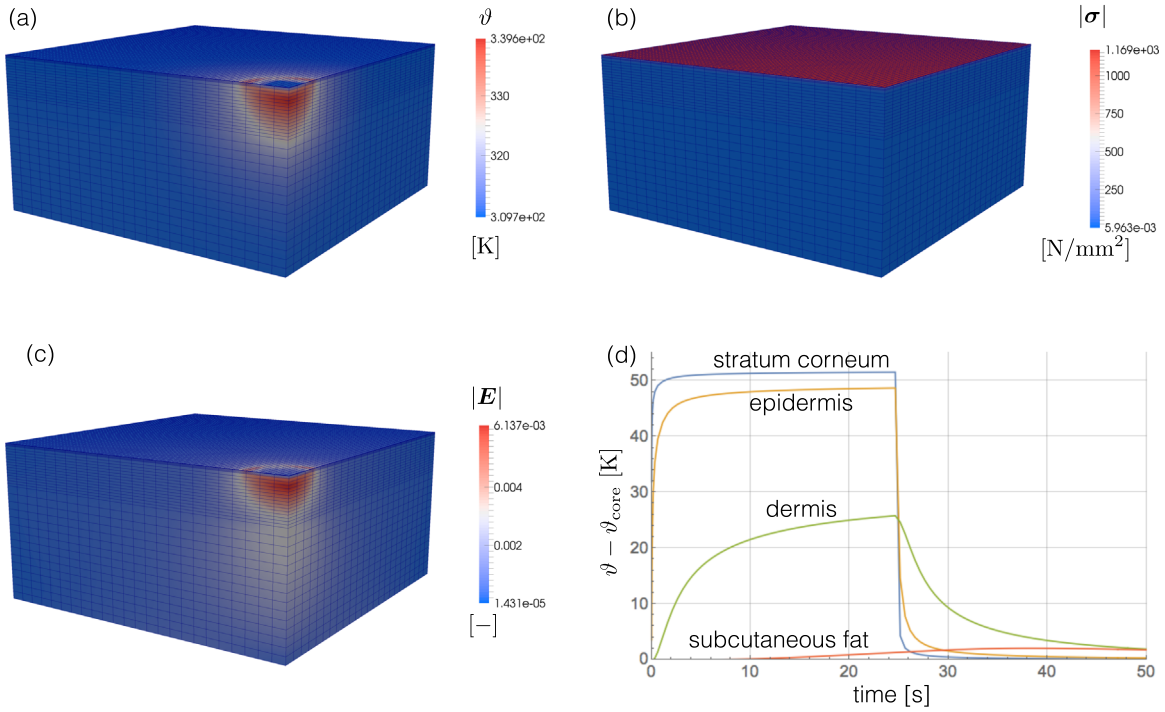

Fig. 5. The variation in the temperature ϑ, the norm of the Cauchy stress tensor $\boldsymbol{\sigma}$ and the norm of the Green–Lagrange strain tensor $\boldsymbol{E}$ at the end of loading stage I are shown in (a)-(c) for the thermally-driven problem. The variation in the temperature difference $\vartheta - \vartheta_{\text{core}}$ at the centre of the various layers of the skin along the vertical line A–B is shown in (d).

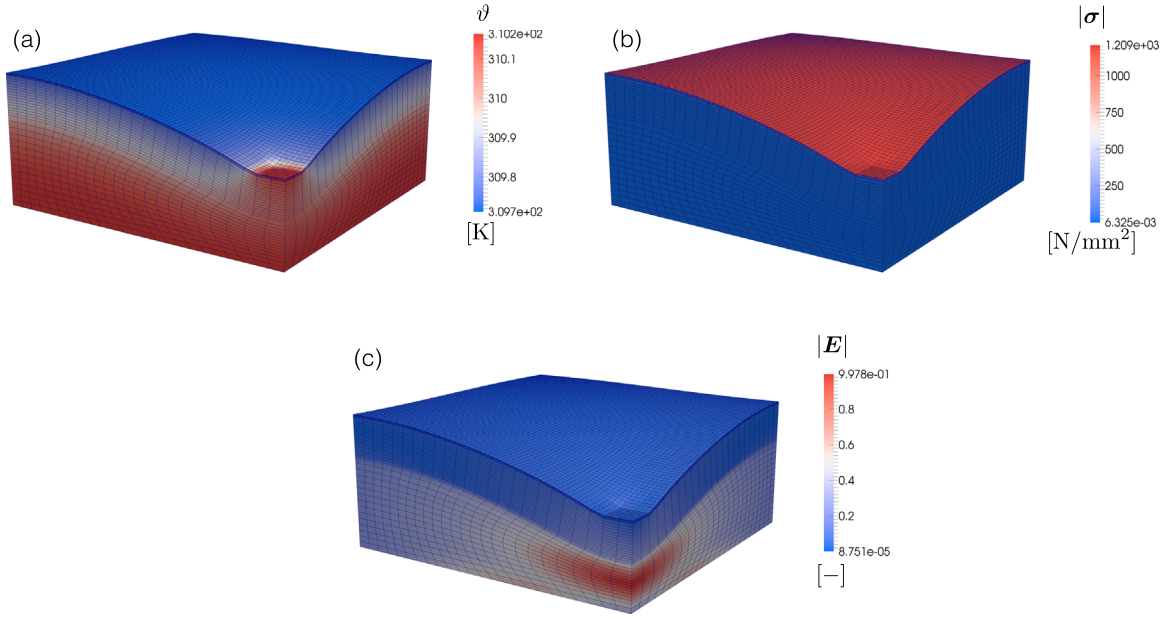

Fig. 6. The variation in the temperature ϑ, the norm of the Cauchy stress tensor $\boldsymbol{\sigma}$ and the norm of the Green–Lagrange strain tensor $\boldsymbol{E}$ at the end of loading stage I are shown in (a)-(c) for the mechanically-driven problem.

the inverse of the right Cauchy–Green tensor in Eq. (9)) is not negligible.

The stress state at the onset of the cooling stage is similar to that in the thermally- and mechanically-driven problem. This indicates the significant contribution of the temperature (via thermal expansion) on the stress state (see Eq. (8)). The thermally induced strains are relatively small but non-negligible.

6.3. *Mechanically-driven problem*

The objective of the mechanically driven problem is to identify how the mechanical loading influences the response of the skin specimen. The temperature of the indenter is now fixed at $\vartheta \equiv \vartheta_{\text{core}}$ during both stage I and II of the loading process. The distribution of the temperature shown in Fig. 6 (a) indicates very little

variation from the reference temperature. The thermoelastic coupling effects (see Eq. (5)) are negligible due to the relatively slow loading rate and the material properties of skin. As was concluded for the thermally-driven problem, It would therefore be appropriate to neglect thermoelastic coupling effects. The distribution of the stress and strain resembles that for the full problem.

7. Discussion and conclusion

A model and aspects of its numerical solution for the fully-coupled nonlinear thermomechanical response of the human skin at finite deformations has been presented. Particular attention was paid to the derivation of the mechanical and thermal constitutive equations as well as their coupling. Although conceptually straightforward, the model extends the formulation of Pennes (1948) to the finite deformation regime using a theoretical approach consistently-grounded in the nonlinear theory of mechanics. Details of the numerical solution scheme using the finite element method in conjunction with automatic differentiation tools were given. A representative numerical example elucidated aspects of the theory and features of the model.

In the full model (i.e. with thermo-mechanical coupling), the stratum corneum and the viable epidermis displayed similar thermal relaxation times. Although unsurprising given their identical thermal conduction, it is worth noting that the thickness of the viable epidermis is four times that of the stratum corneum. In stage I of the simulation, the temperature of the dermis steadily increased until the start of stage II when the trend was immediately reversed while, for the hypodermal layer, the decrease in temperature experienced a delay of about two seconds. This would suggest that, for high thermal load applied to the skin surface, it might be possible to obtain damaging temperatures within the hypodermis even after removal of these loads. It is likely that, if the sub-cutaneous layer experiences a critically high temperature, the epidermal and dermal layers have already exceeded their damage threshold. A direct sensitivity analysis of these aspects should be considered in future studies (see e.g. (Korelc, 2009)).

Despite its small thickness, the mechanical contribution of the stratum corneum during indentation was shown to be significant due to the high value for the Youngs modulus used in our study (about 2 GPa). Similar findings were recently reported by Leyva-Mendivil et al. (2015, 2016) in the context of finite element studies although they used a maximum value of 370 MPa for the elastic modulus of the stratum corneum. The value of 2 GPa corresponds to the higher end of what has been reported in the literature.

It is well established that the stiffness of the stratum corneum decreases with relative humidity due to the plasticisation effect of water (Wu et al., 2006). In reality, this softening of the stratum corneum would be accompanied by swelling which would significantly alter its contact properties with external surfaces in terms of adhesion, deformation-induced friction and, importantly for thermal exchanges, contact area and surface topography. These particular aspects were not captured in the present model.

An obvious extension of the model would be to account for the complex microstructure by incorporating the critical role of collagen fibres via an anisotropic constitutive model. The implementation of the mechanical model poses no significant additional complexity. However, the dependence of the free energy on the temperature needs to be carefully considered, particularly the anisotropic properties of the heat conductivity and capacity. Additional complexity could easily be incorporated into the model to capture, for example, the possible poro-viscoelastic response of the human skin. The next significant extension would be to account for permanent damage due to heating. Prior to this however, careful validation against experimental data is critical. The major challenges lie in the experimental characterisation of the mechanical and thermal properties of the skin across spatial and temporal scales whilst accounting for inter- and intra-individual variability.

In summary, this study proposed a thermodynamically-consistent theoretical and numerical constitutive framework to model the thermomechanical behaviour of human skin for arbitrary kinematics. Thermal blood perfusion and metabolic supply were accounted for and the capabilities/characteristics of the model were demonstrated through a series of examples. This research is a first attempt at providing a numerical assay in the form of a robust modelling framework to assist researchers in developing a more integrated understanding of the complex thermomechanical phenomena that can occur in a variety of physiological, abnormal and traumatic situations.

Acknowledgements

AM acknowledges the support provided by the National Research Foundation through the South African Research Chair in Computational Mechanics. A part of this work was undertaken while AM was visiting the Hamburg University of Technology. AM, DP and GL also acknowledge the financial support provided by the Royal Society via a Newton Fund mobility grant.

References

Bedin, L., Bazán, F.V., 2014. On the 2D bioheat equation with convective boundary conditions and its numerical realization via a highly accurate approach. Appl. Math. Comput. 236, 422–436.
Beradi, G., Jaeger, M., Martin, R., 1996. Modelling of a thermo-viscoelastic coupling for large deformations through finite element analysis. Int. J. Heat Mass Transf. 39 (18), 3911–3924.
Bischoff, J., Arruda, E., Grosh, K., 2002. A microstructurally based orthotropic hyperelastic constitutive law. J. Appl. Mech. 69 (5), 570–579.
Bischoff, J., Kuhl, E., Arruda, M., Grosh, K., 2000. Finite element modeling of human skin using an isotropic, nonlinear elastic constitutive model. J. Biomech. 33 (6), 645–652.
Burns, T., Breathnach, S., Cox, N., Griffiths, C., 2004. Rook's Textbook of Dermatology, 7th ed. Blackwell Science, Oxford.
Choudhary, S., Elsaie, M.L., Leiva, A., Nouri, K., 2010. Lasers for tattoo removal: a review. Lasers Med. Sci. 25 (5), 619–627.
Dehghan, M., Sabouri, M., 2012. A spectral element method for solving the Pennes bioheat transfer equation by using triangular and quadrilateral elements. Appl. Math. Model. 36 (12), 6031–6049.
Garikipati, K., Arruda, E., Grosh, K., Narayanan, H., Calve, S., 2004. A continuum treatment of growth in biological tissue: the coupling of mass transport and mechanics. J. Mech. Phys. Solids 52 (7), 1595–1625.
Gefen, A., 2011. How do microclimate factors affect the risk for superficial pressure ulcers: a mathematical modeling study. J. Tissue Viability 20 (3), 81–88.
Ghazanfarian, J., Saghatchi, R., Patil, D., 2015. Implementation of smoothed-particle hydrodynamics for non-linear pennes' bioheat transfer equation. Appl. Math. Comput. 259, 21–31.
Gurtin, M., 2003. An Introduction to Continuum Mechanics. Elsevier Science, Academic Press, San Diego.
Hassanpour, S., Saboonchi, A., 2014. Interstitial hyperthermia treatment of countercurrent vascular tissue: a comparison of models Pennes, WJ and porous media bioheat models. J. Therm. Biol. 46, 47–55.
Holzapfel, G.A., 2000. Nonlinear Solid Mechanics: A Continuum Approach for Engineering. John Wiley& Sons Ltd,, New York.
Khunger, N., Molpariya, A., Khunger, A., 2015. Complications of tattoos and tattoo removal: stop and think before you ink. J. Cutan. Aesthet. Surg. 8 (1), 30–36.
Knapik, J.J., Reynolds, K.L., Duplantis, K.L., Jones, B.H., 1995. Friction blisters. Pathophysiology, prevention and treatment. Sports Med. 20 (3), 136–147.
Korelc, J., 2002. Multi-language and multi-environment generation of nonlinear finite element codes. Eng. Comput. 18 (4), 312–327.
Korelc, J., 2009. Automation of primal and sensitivity analysis of transient coupled problems. Comput. Mech. 44 (5), 631–649.
Kreidstein, M.L., Giguere, D., Freiberg, A., 1997. MRI interaction with tattoo pigments: case report, pathophysiology, and management. Plast. Reconstr. Surg. 99 (6), 1717–1720.
Kuperman-Beade, M., Levine, V.J., Ashinoff, R., 2001. Laser removal of tattoos. Am. J. Clin. Dermatol. 2 (1), 21–25.

Lakhssassi, A., Kengne, E., Semmaoui, H., 2010. Modifed pennes' equation modelling bio-heat transfer in living tissues: analytical and numerical analysis. Nat. Sci. 2 (12), 1375–1385.
Lang, J., Erdmann, B., Seebass, M., 1999. Impact of nonlinear heat transfer on temperature control in regional hyperthermia. Biomed. Eng., IEEE Trans. 46 (9), 1129–1138.
Leyva-Mendivil, M.F., Page, A., Bressloff, N.W., Limbert, G., 2015. A mechanistic insight into the mechanical role of the stratum corneum during stretching and compression of the skin. J. Mech. Behav. Biomed. Mater. 49, 197–219.
Leyva-Mendivil, M.F., Page, A., Bressloff, N.W., Limbert, G., 2016. Skin microstructure is a key contributor to its friction behaviour. Tribol. Lett., Submitted for publication
Limbert, G., 2011. A mesostructurally-based anisotropic continuum model for biological soft tissues decoupled invariant formulation. J. Mech. Behav. Biomed. Mater. 4 (8), 1637–1657.
Limbert, G., 2014. Computational Biophysics of the Skin. Pan Stanford, Boca Raton, pp. 95–131, Ch. 4.
Pennes, H., 1948. Analysis of tissue and arterial blood temperatures in the resting human forearm. J. Appl. Physiol. 1 (2), 93–122.
Querleux, B., (Ed.), 2014. Computational Biophysics of the Skin. Pan Stanford Publishing.
Ratovoson, D., Huon, V., Costalat, V., Jourdan, F., 2011. Combined model of human skin – heat transfer in the vein and tissue: experimental and numerical study. Quant. InfraRed Thermogr. J. 8 (2), 165–186.
Ross, J.R., Matava, M.J., 2011. Tattoo-induced skin burn during magnetic resonance imaging in a professional football player: a case report. Sports Health 3 (5), 431–434.
Shen, W., Zhang, J., Yang, F., 2005. Modeling and numerical simulation of bioheat transfer and biomechanics in soft tissue. Math. Comput. Model. 41 (11–12), 1251–1265.
Sulzberger, M.B., Cortese, T.A., Fishman, L., Wiley, H.S., 1966. Studies on blisters produced by friction. I. Results of linear rubbing and twisting technics. J. Investig. Dermatol. 47 (5), 456–465.
Tepole, A., Gosain, A., Kuhl, E., 2012. Stretching skin: the physiological limit and beyond. Int. J. Non-Linear Mech. 47 (8), 938–949.
Wu, K.S., van Osdol, W.W., Dauskardt, R.H., 2006. Mechanical properties of human stratum corneum: effects of temperature, hydration, and chemical treatment. Biomaterials 27, 5.
Xu, F., Lu, T., 2011. Introduction to Skin Biothermomechanics and Thermal Pain. Springer, Beijing.
Xu, F., Wen, T., Lu, T., Seffen, K., 2008. Skin biothermomechanics for medical treatments. J. Mech. Behav. Biomed. Mater. 1, 172–187.
Zhao, J., Zhang, J., Kang, N., Yang, F., 2005. A two level finite difference scheme for one dimensional Pennes' bioheat equation. Appl. Math. Comput. 171 (1), 320–331.